Energy Conversion and Management 326 (2025) 119476

Contents lists available at ScienceDirect

Energy Conversion and Management

journal homepage: www.elsevier.com/locate/enconman

Research paper

Optimal control of a bio-based phase change material thermal energy storage for demand response

Aneesh Chandra Nunna [a,b], Olav Galteland [c], Laurent Georges [b], Yi Zong [a,*]

[a] Department of Wind and Energy Systems, Technical University of Denmark, Denmark
[b] Department of Energy and Process Engineering, Norwegian University of Science and Technology, Norway
[c] Department of Thermal Energy, SINTEF Energy Research, Norway

ARTICLE INFO

Keywords:
Demand flexibility
Optimal control
Phase change material
Thermal energy storage

ABSTRACT

In this study, the design and development of an optimal control strategy for the operation of an innovative bio-wax phase change material based pillow plate thermal energy storage unit delivering space heating to a four-storey-high research building is presented. The hydronic heating system in the ZEB-laboratory comprises an electric driven heat pump, the thermal storage unit and hydronic radiators. Numerical control-oriented dynamic models to simulate the phase-change dynamics of the thermal system are developed and validated. To predict the hourly heating load of the building reliably and accurately, a 14-node Resistance–Capacitance thermal network model is developed to be employed as a decision support tool. An optimal model-based predictive control strategy based on the validated system models is developed for application in real-time operation of the thermal storage unit. The control strategy is designed to optimally utilize the energy storage capability of the thermal energy storage unit to generate demand flexibility in response to time-varying electricity price signals. In comparison to a rule based control, the developed optimal control demonstrates a high degree of flexibility – as quantified by values of flexibility factor close to 1 being obtained – indicating a system operating with maximum flexibility, during one month of operation. Further, results demonstrate the availability of storage capacity of 100 kW h–200 kW h per day on average, indicating the capability of the optimized operation of the thermal energy storage unit to provide grid ancillary services. In addition to being demand flexible, the optimal charging schedule reduces the energy consumption and cost by about 40% – 50% on average. Thus, the developed optimal control strategy demonstrates a significant capability to generate and maximize demand flexibility to shift loads intelligently, provide grid services, and reduce energy cost and consumption.

1. Introduction

The European Union (EU) aims to achieve climate neutrality by 2050 [1]. Achieving this objective necessitates a shift away from fossil fuels and towards the adoption of Renewable Energy Sources (RES), notably wind and solar. While RES have the potential to satisfy all the primary energy requirements, their intrinsic intermittency can negatively impact the operation of the power system. The stochastic nature of RES leads to a greater volatility in the power system and thus, an increase in the mismatch between supply and demand [2]. The building sector is the largest energy consuming sector in the EU, accounting for more than one third of the total final energy consumption [3]. A significant part of this building energy demand can be shifted in time to provide flexibility in the energy system and mitigate the issue of demand-supply mismatch.

Energy flexibility in buildings is defined as "the ability of a building to manage its demand and generation in response to local climatic conditions, user needs, and grid requirements" [4]. It is identified as a critical resource to support the transition towards a sustainable power system with high penetration of fluctuating RES [5]. Demand response (DR) in buildings harnesses the potential energy flexibility available in buildings by intelligent management of fluctuations in net load through dynamic adjustment of demand with the variable supply of RES [6]. Further, it allows for the provision of grid services which positively impact the reliability of the power system and thus enable a greater integration of RES [7]. The capability of buildings to provide DR depends on multiple factors [8]: 1. its physical properties such as thermal mass, insulation and geometry, 2. its technologies such as heating system, ventilation and storage devices, 3. its control system,

* Corresponding author.
E-mail addresses: anecha@dtu.dk (A.C. Nunna), olav.galteland@sintef.no (O. Galteland), laurent.georges@ntnu.no (L. Georges), yizo@dtu.dk (Y. Zong).

https://doi.org/10.1016/j.enconman.2024.119476
Received 13 July 2024; Received in revised form 5 December 2024; Accepted 30 December 2024
Available online 8 January 2025

if it has the possibility to react to external signals such as electricity prices, 4. user behaviour and comfort requirements.

As the megatrend of electrification continues to shape the energy system, it is becoming increasingly important to couple the electrical energy with other forms of energy to accelerate the transition to climate neutrality and achieve net-zero goals [9]. Particularly relevant for buildings, is the coupling between the power and heat sectors which is considered to be amongst the most promising sector-coupling options due to the relatively low costs of heat storage and electricity generation from heat [10]. Utilizing renewable electricity to satisfy building heat demand could be significant in the efforts to decarbonize the heating sector as it is well documented that heat demand in buildings comprise the biggest share of total building energy consumption in cold climates. Østergaard et al. [11] estimate that space heating represents around 60%–70% of the total heating demand of buildings. In buildings where domestic hot water consumption is minimal, such as office buildings, space heating can amount up to 90% of the total heat demand.

In buildings equipped with Power-to-Heat (P2H) devices, such as Heat Pumps (HPs), and Thermal Energy Storage (TES) devices, a large potential to generate flexibility is identified through intelligent use of TES devices to accumulate electrical energy in the form of thermal energy through electric HPs connected to the district heating system [12]. TES devices enable the capture and storage of energy during low-demand periods and release energy during high-demand periods, thus decoupling energy demand from its supply [13]. They reduce the discrepancy between demand and supply, improve thermal reliability and efficiency of the system, reduce peak loads and allow greater integration of RES [14]. They are identified as the most mature and effective technology for achieving DR in buildings [15]. Further, buildings can be made grid-interactive through the active utilization of TES devices for space heating.

Thermal energy in TES devices can be stored in three forms: sensible heat, latent heat and thermochemical heat storage. Amongst the three, latent heat TES using Phase Change Materials (PCMs) are identified as one of the better suited technologies due to their versatility, economic viability and industrial maturity [16]. PCMs undergo reversible phase transition – usually between solid and liquid phases – upon thermal action i.e. they absorb heat during melting and release heat during solidification and crystallization [17]. The energy storage density in these transitions is considerably higher than sensible heat storage (such as hot water tanks). PCMs, acting as thermal batteries, demonstrate long term stability and reliability as they can store and release thermal energy on demand many thousands of times without a change in their thermal properties [18]. Notably, the phase transition occurs within a narrow temperature range. This has two important benefits: 1. thermal energy can be stored from hot/cold flows only a few degrees above/below the melting temperature and 2. thermal losses are reduced due to smaller temperature differences. To minimize the carbon footprint and improve sustainability, bio-based PCMs, derived from renewable and environmentally friendly resources, are increasingly being deployed in industrial applications [19]. There are several options available for the design of heat exchangers in the TES devices, such as fin-and-tube and plate heat exchangers. Of them, pillow plate heat exchangers are regarded as more favourable for thermal storage applications due to their compactness, durability and higher heat outputs [20].

Predictive control strategies can be employed to actively harness the demand response potential of TES devices. Approaches to activate DR generally require the following: a model capturing the dynamics of the thermal system, a prediction model providing information of the future thermal demand in-advance, external information such as weather forecasts and electricity price signals, and importantly, a control framework to optimize the use of thermal storage [21]. The flexibility generated through these advanced control strategies can be quantified by various performance indicators — such as the flexibility factor and the storage capacity [22]. Finck et al. [23] quantify the demand flexibility of a building heating system integrated with TES and their simulation results show the potential for significant short-term flexibility through the intelligent control of TES devices. Further, Tarragona et al. [24] report that the deployment of such intelligent control strategies can lead to both energy and cost savings when compared with conventional rule-based control strategies.

The literature on DR for TES shows that very few works focus on the application of predictive control for PCM TES devices. Instead, the most common application was for sensible TES devices with water as the energy store. The feasibility of price based predictive control strategy to optimize the operation of a solar thermal heating system integrated with a sensible TES for DR was investigated in [25]. Their results show that the TES can be utilized efficiently to shift the electrical load to target low price periods and achieve electricity cost reductions of more than 60% without compromising the indoor comfort. In another study [26], the participation of sensible TES integrated buildings in DR programmes was investigated and results indicate that the optimal control of TES devices can provide buildings with increased operational flexibility while also significantly reducing building energy costs.

In this paper, an optimal control strategy is developed for an innovative bio-based PCM TES device supplying space heating to a four-storey-high building. The main aim of the developed control is to activate and harness the DR capability of the thermal storage in the context of P2H conversion for building heat demand. The developed control strategy is designed to optimally utilize the TES capability of the system to dynamically shift the heating load based on electricity price signals while satisfying the demand requirements of the users in the building. Further, flexibility indicators are employed to 1. quantify the additional flexibility generated 2. and to identify the capability of providing grid services by the optimal control with reference to a traditional rule-based control. This work contributes to new knowledge on how intelligent control strategies can be implemented to achieve price based DR of buildings equipped with active PCM devices.

Rest of the paper is organized as follows: In Section 2, the ZEB-laboratory is introduced and its thermal system, including the TES unit and hydronic heating system, is described. Section 3 discusses in detail the development of control-oriented numerical models of the various components of the thermal system such as the pillow plate TES, heat pump system and hot water tank. Also, a numerical model for the prediction of space heating demand of the building is developed. The developed numerical models are validated against measurement data and the validation results are presented. In Section 4, the methodology and design of an optimal control strategy is discussed. Flexibility indicators to quantify demand flexibility are introduced to evaluate the performance of the developed control with respect to a rule based control. Section 5 discusses the optimization results and concludes the study.

2. ZEB-laboratory

The ZEB-laboratory, shown in Fig. 1, is located in Trondheim, Norway. It is a four-storey-high building that functions as a living laboratory i.e. as both an office building used by ordinary people and a multipurpose experimental facility that serves as a playground for full-scale research on building energy management technologies and occupant-building interaction [27]. The south, west and east facades of the building along with the roof are integrated with Photo-Voltaic (PV) panels. The building is oriented towards the south with a pitched roof of 30° for efficient utilization of sunlight. Waterborne radiators are installed in each floor to provide space heating. In addition, there are two Heat Recovery Ventilation (HRV) units that are responsible for mechanical ventilation of warm fresh air. The HRV unit comprises an Air Handling Unit (AHU) and a heat recovery exchanger.

An innovative TES unit, in combination with an air-to-water heat pump system, is integrated into the central hydronic heating system of

Table 1
Thermophysical properties of the PPTES unit in the ZEB-laboratory.

Symbol	Description	Value
$L \times W \times H$	Dimensions	$2.250 \times 0.800 \times 1.254$ m
n	Number of pillow plates	24
d_{ins}	Width of Insulation	0.15 m
T_m	Melting temperature of PCM	37.5 °C
Δh_{lat}	Specific latent heat of PCM	198.6 kJ kg^{-1}
$c_{p,l,PCM}$	Specific heat capacity of liquid PCM	1.4 kJ kg^{-1} K^{-1}
$c_{p,s,PCM}$	Specific heat capacity of solid PCM	2.3 kJ kg^{-1} K^{-1}
$c_{p,HTF}$	Specific heat capacity of HTF	4.2 kJ kg^{-1} K^{-1}
$c_{p,PW}$	Specific heat capacity of PW	0.5 kJ kg^{-1} K^{-1}
$\lambda_{l,PCM}$	Thermal conductivity of liquid PCM	0.170 W m^{-1} K^{-1}
$\lambda_{s,PCM}$	Thermal conductivity of solid PCM	0.240 W m^{-1} K^{-1}
λ_{HTF}	Thermal conductivity of HTF	0.598 W m^{-1} K^{-1}
λ_{PP}	Thermal conductivity of PW	15.0 W m^{-1} K^{-1}
λ_{PW}	Thermal conductivity of insulation	0.04 W m^{-1} K^{-1}
$\rho_{l,PCM}$	Mass density of liquid PCM	957 kg m^{-3}
$\rho_{s,PCM}$	Mass density of solid PCM	819 kg m^{-3}
ρ_{HTF}	Mass density of HTF	997 kg m^{-3}
ρ_{PW}	Mass density of PW	8000 kg m^{-3}

the ZEB-laboratory. The thermal system delivers heat to the hydronic radiators, located in each floor, for space heating and also to the HRV units for heating ventilation air [28]. In addition, heat is also delivered to pre-heat domestic hot water. The TES unit can be charged by the heat pump, and it can be discharged to provide heat to the building through the heating system. A simplified process diagram is shown in Fig. 2.

The TES unit comprises a 3200 L tank filled with 3000 kg of PCM and 24 stainless steel pillow plate heat exchangers arranged in parallel. Water, acting as the Heat Transfer Fluid (HTF), circulates in each of the pillow plates following a 2-pass pattern. In this configuration, 90% of the tank-volume is occupied by the PCM. A 150 mm thick thermal insulation around the tank ensures the heat loss is limited to about 1% over a 24 hour period [29]. Figs. 3 and 4 display the PPTES unit and its internal structure respectively. The primary purpose of the TES unit is to act as a thermal battery by actively absorbing, storing and releasing thermal energy on demand.

CrodaTherm™ 37 (CT37) is used as the PCM. It is a water-insoluble organic PCM derived from plant-based feedstocks and has a melting temperature of 37.5 °C. In solid phase it behaves as a crystalline wax while in liquid phase it acts as an oily liquid. It is an optimal material for thermal storage as it has a low melting temperature range (≈1.5 °C), exhibits a low degree of super cooling, has a low-carbon footprint and is affordable [30]. Operational data of the Pillow Plate Thermal Energy Storage (PPTES) unit show that it has a maximum heat storage capacity of 200 kW h, a peak heat output of up to 40 kW, can deliver sustained heat output above 10 kW for several hours and has an energy efficiency of 95% [29]. The thermophysical properties of the PPTES unit have been experimentally validated in previous studies [31] and are presented in Table 1.

The heat pump system consists of two air-to-water heat pumps, each having a thermal capacity of 15 kW, connected in a parallel configuration. The heat delivered by the heat pumps is used to charge the PPTES and accumulate thermal energy, which is then dispatched to provide space heating to the ZEB-laboratory. The heat pump system is nominally designed to handle temperature lifts from 35 °C to 40 °C on the supply side.

A hot water tank, having a volume of 0.8 m^3, is placed on the primary side. It separates the supply side (PPTES and heat pump system) and the demand side (space heating system). It acts as a temporary energy store and provides a buffer between the supply and demand side. However, it can only store the energy required to satisfy the space heating demand for up to 15 minutes. It is charged either by the heat pump or the PPTES, with inflow at the top and outflow at the bottom. During discharge to provide space heating, hot water from the top is supplied to the building and is replaced by cold water return at the bottom.

Table 2
Parameters of the developed numerical model for PPTES unit.

Symbol	Description	Value
m	Number of vertical numerical regions	3
Δt	Time step	60 s
Δx_{PCM}	Width of numerical PCM region	0.042 65 m
Δx_{HTF}	Width of numerical HTF region	0.0043 m
Δx_{PW}	Width of numerical PW region	0.001 m

3. Numerical modelling

In this section, the design and development of control-oriented numerical models for the PPTES, heat pump system, hot water tank and a space heating prediction model of the building are discussed. Measurement data from the various sensors located in the building are used to validate the developed numerical models.

3.1. Thermal storage

A control-oriented numerical model for the PPTES unit has been developed, based on the equivalent heat capacity method [33], to model the local heat and mass transport as well as the phase-change dynamics of the PCM. The model integrates both the PCM and the pillow plates as heat exchangers. The system is simulated on a quasi-two-dimensional basis i.e. transport equations are resolved in a singular dimension for each phase β and a source term is responsible for mediating the heat transfer between the two phases (solid and liquid). The source term also accounts for both the heat absorbed during melting and heat released during solidification of the PCM.

The PPTES unit is discretized vertically into m numerical regions, resulting in $(n+1)\times m$ numerical regions for the PCM and $n \times m$ regions for the HTF, where n is the number of pillow plates. The numerical regions are illustrated in Fig. 5 and their values are listed in Table 2.

The scalar transport equation for both the PCM and HTF temperatures are formulated in Eq. (1), where T is temperature, t is time, λ_β is thermal conductivity, ρ is mass density, $c_{p,\beta}$ is the specific heat capacity, υ is velocity, q is the heat source term accounting for the rate of heat flow to the region and m_β is the mass [34]. In the thin PCM regions, natural convection is neglected and, the velocity is assumed to be zero as the liquid PCM is highly viscous. Hence, the transport equations for the PCM reduce to the heat equation. The velocity of HTF, which is an input to the numerical model, is taken to be uniform as the HTF is assumed to be incompressible. The heat source term in Eq. (2) encompasses the rate of heat transfer between the HTF and the PCM q_{tran}, the rate of heat loss to the environment through the insulation q_{loss}, and the rate at which heat is either absorbed during melting or released during solidification of the PCM q_{melt}. The rate of heat flow between phases q_{tran} and rate of heat loss q_{loss} are modelled by the Fourier's law given in Eq. (3), where A is the surface area, and W is the thickness of the interface between regions or thickness of insulation. The rate of melting and solidification of the PCM is determined by the heat source term q and thus, the liquid fraction x_l of the PCM is temporally dependent on q as described in Eq. (4) where Δh_{lat} is the latent heat of the PCM. The heat source term is modified to take into account heat lost or gained during melting or solidification. The numerical model simulates the following processes:

1. Heat advection and conduction within the HTF region.
2. Heat conduction, as well as the melting and solidification processes, in the PCM region.
3. Heat conduction occurring between neighbouring HTF and PCM regions.

$$\frac{\partial T}{\partial t} = \frac{\lambda_\beta}{\rho c_{p,\beta}} \frac{\partial^2 T}{\partial y^2} - \upsilon \frac{\partial T}{\partial y} + \frac{q}{m_\beta c_{p,\beta}} \tag{1}$$

$$q = q_{tran} + q_{loss} + q_{melt} \tag{2}$$

Fig. 1. The ZEB-laboratory.
Photo: Nicola Lolli/SINTEF.

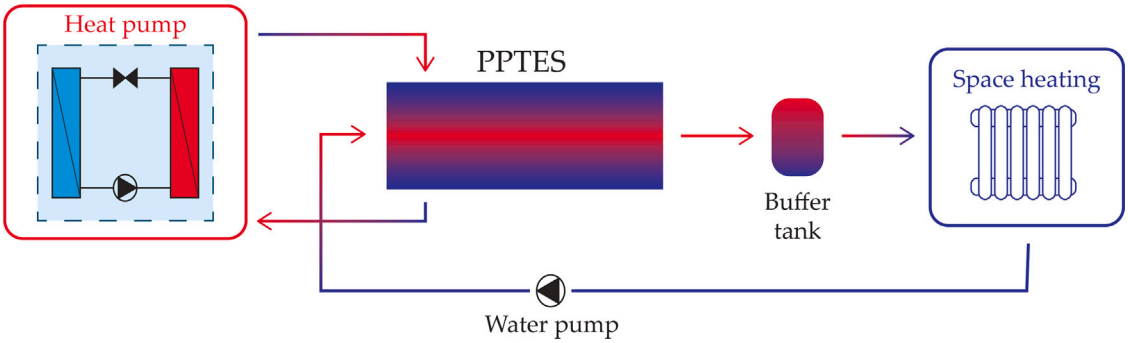

Fig. 2. An overview of the thermal system at the ZEB-laboratory.

Fig. 3. The PPTES unit [32]. It is housed in a thermally insulated container.

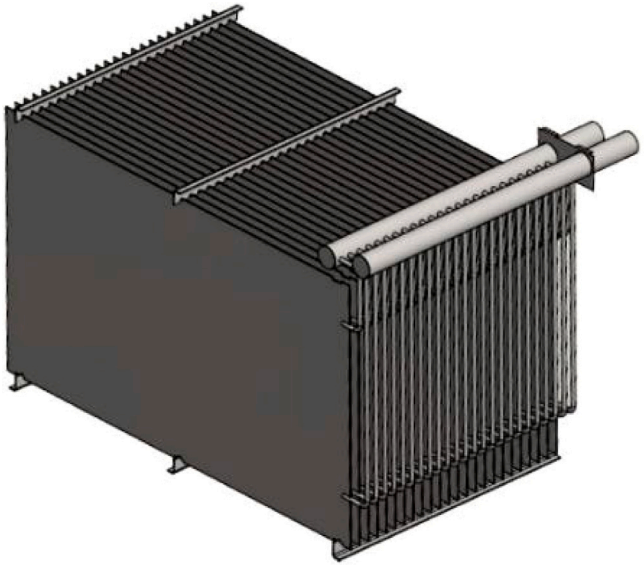

Fig. 4. Internal structure of the PPTES unit showing the parallel pillow plate heat exchangers and, the supply and return water headers [31].

$$q_{\text{tran/loss}} = -\frac{\lambda A}{W}\Delta T \tag{3}$$

$$\frac{\partial x_l}{\partial t} = \frac{q_{\text{melt}}}{\Delta h_{\text{lat}} m_{\text{PCM}}} \tag{4}$$

Dirichlet boundary conditions are used with a ghost-cell method, where the boundary cells are located outside the main domain. At the HTF inlet ghost-cell ($y = -\Delta y$) the temperature is equal to T_{in}, which is the inlet temperature. While at the HTF outlet ghost-cell ($y = L_y + \Delta_y$) the temperature is equal to the adjacent upstream temperature. The boundary of the PCM is with room, therefore the temperature of the ghost-cells adjacent to the PCM is equal to the room temperature T_{room}. Uniform initial temperatures are assumed for both the PCM and the HTF. Eqs. (5)–(9) list the boundary and initial conditions described above.

$$T_{\text{HTF}}(x, y = -\Delta y) = T_{in} \tag{5}$$

$$T_{\text{HTF}}(x, y = L_y + \Delta_y) = T_{\text{HTF}}(x, y = L_y) \tag{6}$$

$$T_{\text{PCM}}(x, y = -\Delta y) = T_{\text{PCM}}(x = L_x + \Delta x, y) = T_{\text{room}} \tag{7}$$

$$T_{\text{PCM}}(t = 0, x, y) = T_{\text{PCM,0}} \tag{8}$$

$$T_{\text{HTF}}(t = 0, x, y) = T_{\text{HTF,0}} \tag{9}$$

The Crank–Nicolson numerical scheme, a widely-recognized implicit method, is employed to numerically discretize the one-dimensional convection–diffusion equation presented in Eq. (1). This scheme offers a balanced combination of both the explicit and implicit methods, ensuring stability and accuracy. Its central-differencing approach provides a consistent and efficient means of handling the temporal evolution in the transport equations, reducing potential oscillations and ensuring smoother results.

Central differencing is used for the second-order conduction term in Eq. (10), while backward difference in Eq. (11) and forward difference in Eq. (12) are used for the advection term (relevant for the HTF region only) and the time derivative respectively. The indices i and j represent time and position, while Δy and Δt represent the spatial and temporal discretization.

$$\frac{\partial^2 T}{\partial y^2} \approx \frac{1}{2(\Delta y)^2}\left(T_{j+1}^{i+1} - 2T_j^{i+1} + T_{j-1}^{i+1} + T_{j+1}^{i} - 2T_j^{i} + T_{j-1}^{i}\right) \tag{10}$$

$$\frac{\partial T}{\partial y} \approx \frac{1}{4\Delta y}\left(T_j^{i+1} - T_{j-1}^{i+1} + T_j^{i} - T_{j-1}^{i}\right) \tag{11}$$

$$\frac{\partial T}{\partial t} \approx \frac{T_j^{i+1} - T_j^{i}}{\Delta t} \tag{12}$$

The discrete form of Eq. (1) is thus obtained in Eq. (13). It is further reformulated into a set of tri-diagonal linear equations in Eq. (14) of the form $ax_{j-1} + bx_j + cx_{j+1} = d$, where $a = -(r + s)$, $b = (1 + 2r + s)$, $c = -r$ and $d = (r + s)T_{j-1}^{i} + (1 - 2r - s)T_j^{i} + rT_{j+1}^{i} + g$, which can be efficiently solved using the tri-diagonal matrix algorithm.

$$\begin{aligned}\frac{(T_j^{i+1} - T_j^{i})}{\Delta t} &= \frac{\lambda_\beta}{2\rho c_{p,\beta}(\Delta y)^2}\left(T_{j+1}^{i+1} - 2T_j^{i+1} + T_{j-1}^{i+1} + T_{j+1}^{i} - 2T_j^{i} + T_{j-1}^{i}\right) \\ &- \frac{v_\beta}{4\Delta y}\left(T_j^{i+1} - T_{j-1}^{i+1} + T_j^{i} - T_{j-1}^{i}\right) + \frac{q}{m_\beta c_{p,\beta}}\end{aligned} \tag{13}$$

$$\begin{aligned}&-(r + s)T_{j-1}^{i+1} + (1 + 2r + s)T_j^{i+1} - (r)T_{j+1}^{i+1} \\ &= (r + s)T_{j-1}^{i} + (1 - 2r - s)T_j^{i} + (r)T_{j+1}^{i} + g\end{aligned} \tag{14}$$

$$r = \frac{\lambda_\beta}{2\rho c_{p,\beta}(\Delta y)^2}$$

$$s = \frac{v_\beta}{4\Delta y}$$

$$g = \frac{q}{m_\beta c_{p,\beta}}$$

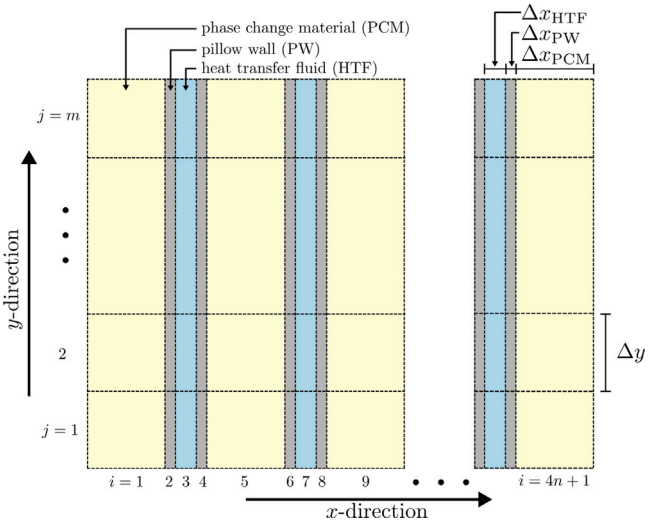

Fig. 5. Illustration of the numerical regions of the PPTES model.

3.1.1. Validation

Two cases are investigated for validating the developed numerical model:

1. A charge–discharge cycle over a period of 85 h.
2. A heat loss experiment over a period of 250 h.

In Figs. 6 and 7, the simulation results of the developed numerical model are plotted against sensor measurements. It is observed that the numerical model is able to simulate the temperature dynamics of the PCM and HTF regions during the phase-transition to a high accuracy (±1 °C), while a greater inaccuracy in modelling the HTF temperatures is observed when the PCM is in sensible heat mode. As the developed model is intended primarily to model the dynamics of the PPTES unit during the latent heat mode, the greater error observed during sensible heat mode is ignored. Significantly, the thermal power delivered and absorbed, and the thermal energy stored in the PCM are modelled to a greater accuracy, in both the latent and sensible mode of the PCM. The thermal power and thermal energy stored are more relevant than the temperature states for developing a predictive control strategy that seeks to utilize the TES capability of the PPTES in an optimal fashion. Further, the numerical model is able to closely match the rate of heat loss observed over 10 days, despite assuming a fixed temperature of 21 °C for the room housing the PPTES unit, which in-reality varies between 17 °C–23 °C. Therefore, the simulation results show that the developed numerical model is able to simulate the dynamics of the PPTES with sufficient accuracy. The developed model is thus validated and can be deployed in a predictive control strategy as a decision support tool.

3.2. Heat pump

A data-driven numerical model of the combined heat pump system is developed to accurately model the flow temperature T_{flow} on the supply side and the electrical consumption of the compressor P_{el}, which are the relevant parameters for optimal control. Models for the COP (Coefficient Of Performance) and T_{flow} are obtained by regression on the measurement data, using the return temperature T_{ret} and external air temperature T_{e} as the predictors. The regression coefficients are listed in Table 3.

$$T_{\text{flow}} = a_0 \cdot T_{\text{e}} + a_1 \cdot T_{\text{ret}} + a_2 \tag{15}$$

$$\text{COP} = b_0 \cdot T_{\text{e}} + b_1 \tag{16}$$

$$P_{\text{el}} = \frac{\dot{m} \cdot c_p \cdot (T_{\text{flow}} - T_{\text{ret}})}{\text{COP}} \tag{17}$$

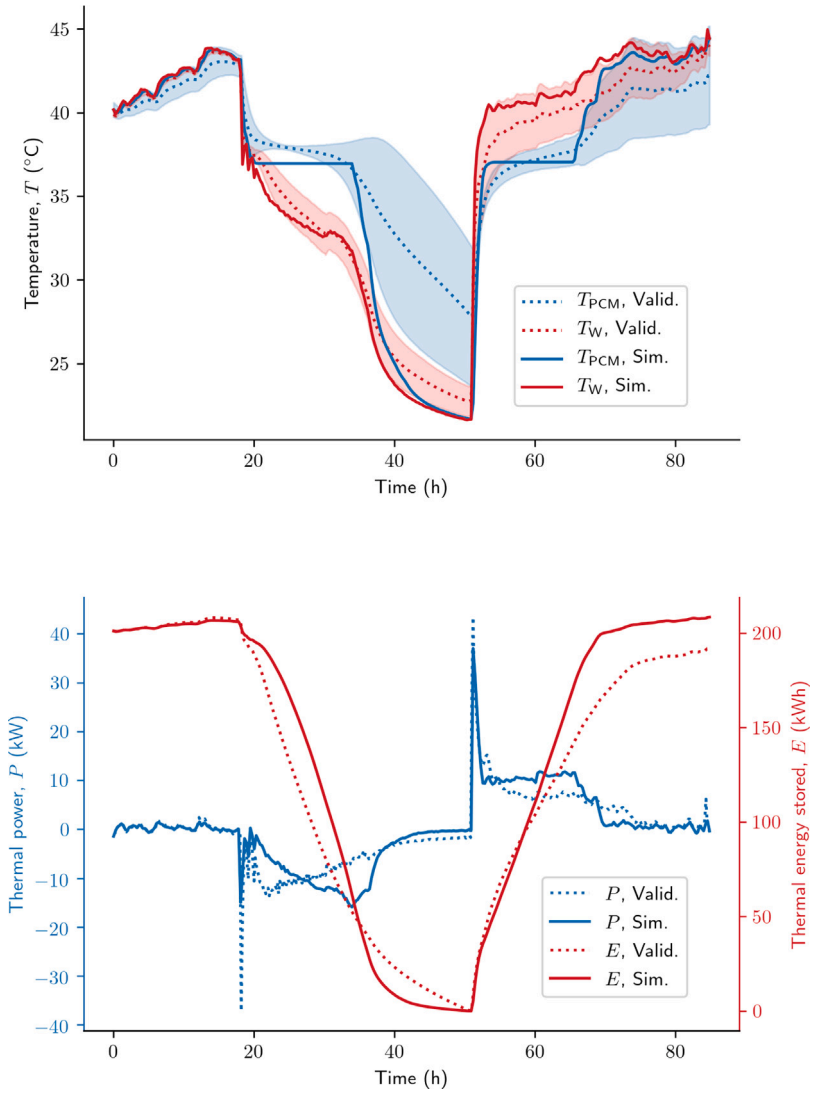

Fig. 6. Validation of the PPTES numerical model over a full discharge–charge cycle over a period of 85 h. The dotted lines are measurements while the solid lines are the simulation data. Top: Temperature of the PCM in blue and HTF in red. The coloured areas illustrate the standard deviation of the validation data. Bottom: Thermal power in blue and thermal energy stored in red.

Table 3
Regression coefficients of the heat pump numerical model.

a_0	a_1	a_2	b_0	b_1
0.096	0.990	4.387	0.044	2.491

3.2.1. Validation

The developed models for the T_{flow}, COP and P_{el} are validated against measurement data. The data includes the measurements of relevant parameters during the operational phase of the heat pumps i.e. when they are switched ON for at least 15 minutes to avoid transient behaviour during start-up and shut-down. The validation results are shown in Fig. 8. The models are found to be reasonably accurate which is shown by the low value of the RMSE (Root Mean Squared Error) of the residual errors. Higher accuracy is obtained in predicting the two parameters that are important for optimal control — flow temperature (RMSE = 0.6 °C) and electrical power consumption (RMSE = 0.3 kW), while a slightly lower accuracy is obtained in modelling the COP (RMSE = 0.3).

3.3. Water tank

A numerical model for the thermally stratified buffer tank that includes heat and mass transfer by conduction and convection is developed. The tank is discretized in the vertical direction into n nodes. Mass and energy balance equations are formulated for each node to obtain a system of Ordinary Differential Equations (ODEs) that capture the tank dynamics. The temporal evolution of nodal temperatures T_i are obtained by solving the ODE formulated in Eq. (18). The terms $\dot{Q}_{ambient}$, $\dot{Q}_{free,i}$ and $\dot{Q}_{forced,i}$ represent the heat loss to ambient, heat transfer due to natural convection and heat transfer due to forced mass transfer respectively, where $\dot{m}_i$ is the nodal mass flow, U_{eff} is the effective thermal transmittance of the tank wall, r and h are the radius and height of tank, and λ_{eff} is the effective vertical heat conductivity. The geometry of the tank and the parameters of the model are listed in Table 4.

As there are no temperature sensors measuring the water temperatures within the tank, it is not possible to validate the developed numerical model. However, during simulations, it is observed that the temperature of the top node closely matches the measured temperature of hot water supply to the building on the secondary side. Moreover, several studies have employed similar models to accurately model the

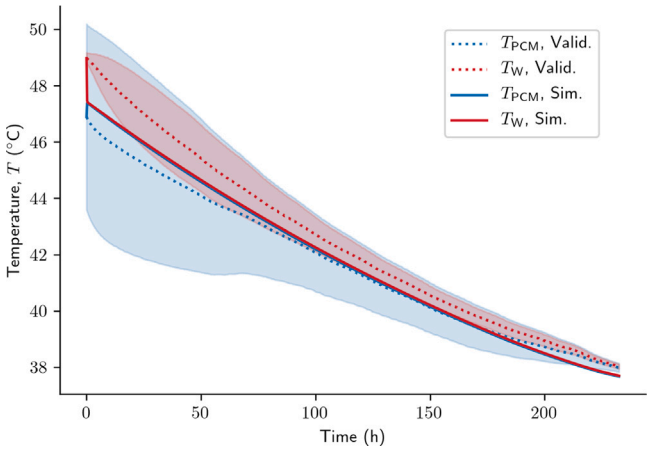

Fig. 7. Validation of the PPTES numerical model during a heat loss experiment over a period of 250 h. The dotted lines are measurements while the solid lines are the simulation data. Temperature of the PCM in blue and HTF in red during a heat loss over 250 h.

Table 4
Geometry and parameters of the tank numerical model.

r (m)	h (m)	n	λ_{eff} (W m^{-1} K^{-1})	U_{eff} (W m^{-2} K^{-1})	T_{amb} (°C)
0.503	1.006	3	1.0	0.45	20

observed thermal stratification and thermal dynamics. Therefore, the developed numerical model of the tank is considered to be reasonably accurate, even though it is not possible to measure the model performance with respect to the nodal temperature estimates.

$$\dot{m}_i c_p \frac{\mathrm{d}T_i}{\mathrm{d}t} = \dot{Q}_{\text{inj},1} + \dot{Q}_{\text{amb},i} + \dot{Q}_{\text{free},i} + \dot{Q}_{\text{forced},i} - \dot{Q}_{\text{inj},n} \tag{18}$$

$$\dot{Q}_{\text{amb},i} = -U_{\text{eff}} \cdot A_i \cdot (T_i - T_{\text{amb}}) \tag{19}$$

$$\dot{Q}_{\text{free},i} = \frac{\pi r^2 n \cdot \lambda_{\text{eff}}}{h} \cdot (T_{i-1} - 2 \cdot T_i + T_{i+1}) \tag{20}$$

$$\dot{Q}_{\text{forced},i} = \dot{m}_i \cdot c_p (T_{i-1} - T_i) + \dot{m}_{i+1} \cdot c_p \cdot (T_i - T_{i+1}) \tag{21}$$

$$\dot{Q}_{\text{inj},i} = \dot{m}_i \cdot c_p \cdot (T_{\text{in}} - T_i) \tag{22}$$

3.4. Space heating demand

A numerical model for reliably estimating the hourly building energy need is developed based on the modelling framework presented in [35]. The framework is based on the ISO 52016-1:2017 standard [36] and employs a 14-node Resistance–Capacitance (RC) thermal network (ISO14N) model to estimate hourly internal temperatures and, heating and cooling loads. Construction elements of the building (such as roof, external walls, etc.) are lumped by type and are represented as serially connected RC elements having one or more temperature nodes.

The opaque building elements – roof rf, ground floor gf and the external walls ew – are modelled as lumped 3-node elements while the internal mass im and window glazing gl elements are modelled as lumped 2-node elements. The internal air node, having a single temperature node, represents the indoor temperature by considering the whole building as a single zone. The thermal RC network diagram of the ISO14N is visualized in Fig. 9. The thermal model of this network is represented numerically by a system of equations of the form:

$$A \cdot \boldsymbol{T}_t = b_{t-1} \tag{23}$$

where $\boldsymbol{T} \in \mathbb{R}^{14}$ is the temperature state vector, $A \in \mathbb{R}^{14\times14}$ is the system coefficient matrix and $b \in \mathbb{R}^{14}$ is a vector containing known terms: temperature state at previous time step and boundary conditions.

The system of equations are solved for each time step to obtain the temperature dynamics. The mathematical formulation of the system coefficients and the boundary conditions of the system are briefly detailed below. For a full description of the structure of matrices A and b, the reader is referred to Lundström et al. [35].

3.4.1. Heat transfer coefficients

Correlation equations for convectional surface heat transfer coefficients of exterior surfaces h_{ce}, displayed in Eq. (24), take into account local weather conditions, wind sheltering effects [37] and surface roughness [35]. The surface of the roof is taken to be smooth ($R_{f,rf} = 1.11$) while external walls are considered to be medium rough ($R_{f,ew} = 1.52$). A constant value for the natural convective heat transfer coefficient ($h_{c,n} = 2.7\,\text{W m}^{-2}\,\text{K}^{-1}$) is assumed by fixing the temperature difference between external air and exterior surface of the building element ($\Delta T = 5\,°\text{C}$). The forced convective heat transfer coefficients h_{cf} in Eqs. (25) and (26) are strongly dependent on the local wind speed U_{loc} as well as the fraction of wind-ward oriented external surfaces F_{ww}. The ZEB-laboratory belongs to shelter class 3 as defined in [38], and thus the corresponding plan area density value is obtained as $\lambda_p = 0.11$. The local wind speed for horizontal and vertical elements is obtained from Eq. (27) where H is the building height and, $\alpha = 0.22$ and $\delta = 370$ are the atmospheric boundary layer coefficients for urban terrain and, U_{10m} is the meteorological wind speed at 10 m height.

$$h_{ce,el}(t) = \begin{cases} h_{c,n} + R_{f,el}\left(\sqrt{h_{c,n}^2 + h_{cf,hor}(t)^2} - h_{c,n}\right) & \text{if } el = rf \\ h_{c,n} + R_{f,el}\left(\sqrt{h_{c,n}^2 + h_{cf,ver}(t)^2} - h_{c,n}\right) & \text{if } el = ew \\ \sqrt{h_{c,n}^2 + h_{cf,ver}(t)^2} & \text{if } el = gl \end{cases} \tag{24}$$

$$h_{cf,ver}(t) = \left[F_{ww} \cdot (3.39 - 5.03 \cdot \lambda_p) + (1 - F_{ww})(1.15 + 0.82 \cdot \lambda_p)\right] \cdot U_{loc,ver}(t)^{0.94} \tag{25}$$

$$h_{cf,hor}(t) = \left[3.57 + 1.72 \cdot \lambda_p\right] \cdot U_{loc,hor}(t)^{0.84} \tag{26}$$

$$U_{loc}(t) = 1.59 \left(\frac{H}{\delta}\right)^{\alpha} U_{10m}(t) \tag{27}$$

The normalized heat transfer coefficient $H_{se,el}$ between the exterior surface node of the element and external air is defined in Eq. (28) for the exterior building elements. It models the heat transfer due to both convective and radiative effects. The exterior radiative heat transfer coefficient is taken to be constant ($h_{re,el} = 4.14\,\text{W m}^{-2}\,\text{K}^{-1}$). The value for the sky-view factor F_{sky} depends on the orientation of the building element (0.5 for vertical elements and 1.0 for horizontal elements). The coefficients are normalized to per m^2 of floor area through the geometrical ratios r_{el}, which are given as the ratio between the total interior surface area of the element to the total floor area of the building [39]. The ratios can be readily computed using building data such as the perimeter P, number of floors N_{fl} and the area A_{fl} of each floor. $h_{gr,vi}$ denotes the thermal transmittance of a virtual ground layer [40].

The distribution of local wind speed and direction, illustrated in Fig. 10, provides an overview of the dominant wind directions, which are seen to be south and west for the ZEB-laboratory, and determine the fraction of wind-ward oriented exterior surfaces ($F_{ww} = 0.49$, corresponding to the north and east facades of the building).

$$H_{se,el}(t) = \begin{cases} r_{el}\left[h_{ce,el}(t) + (1 - F_{sky,hor}) \cdot h_{re,el}\right] & \text{if } el = rf \\ r_{el} \cdot h_{gr,vi} & \text{if } el = gf \\ r_{el}\left[h_{ce,el}(t) + (1 - F_{sky,ver}) \cdot h_{re,el}\right] & \text{if } el \in \{ew, gl\} \end{cases} \tag{28}$$

$$H_{ci,el} = r_{el} \cdot h_{ci,el} \tag{29}$$

$$H_{ri,el} = r_{el} \cdot h_{ri,el} \tag{30}$$

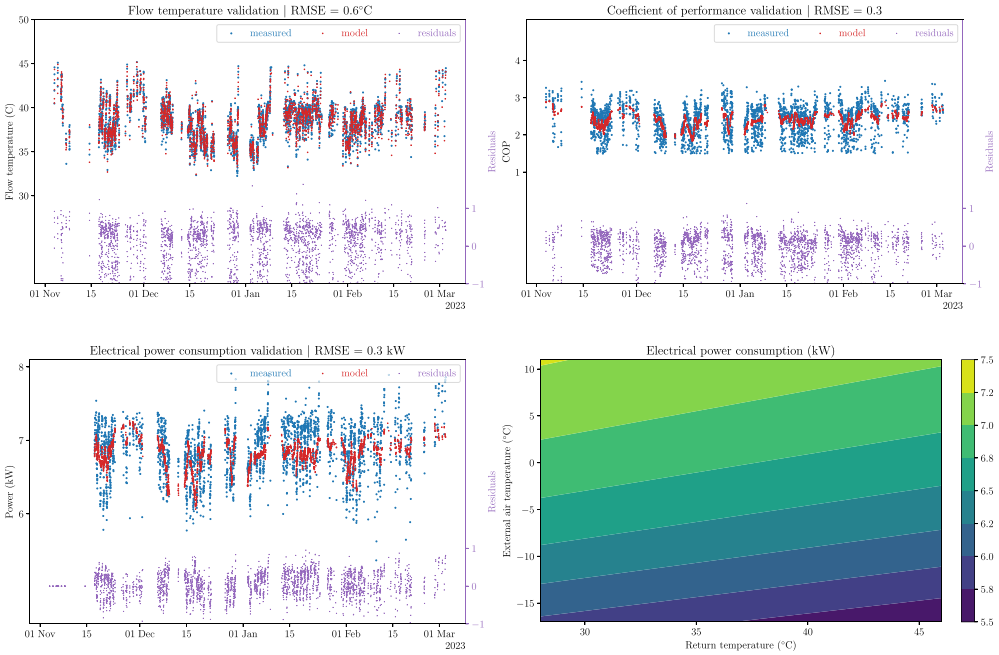

Fig. 8. Validation of the heat pump numerical model. The measurement data are plotted against the model results. The residual errors are shown along with their RMSE score. Top left: Flow temperature. Top right: COP. Bottom left: Electrical power. Bottom right: Contour map of P_{el} with respect to T_{ret} and T_e.

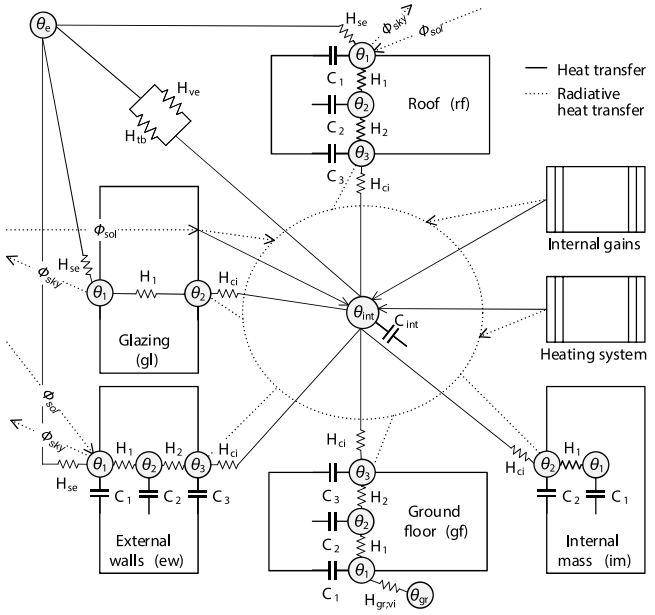

Fig. 9. The thermal RC network of the ISO14N modelling framework [35].

$$r_{el} = \begin{cases} 1/N_{fl} & \text{if } el \in \{rf, gf\} \\ \dfrac{P \cdot H}{\sum A_{fl}} - r_{gl} & \text{if } el = ew \\ 3.5 - \dfrac{2}{N_{fl}} & \text{if } el = im \end{cases} \tag{31}$$

Similarly, the normalized radiative and convective heat transfer coefficients between the interior surface nodes and internal air node are described in Eqs. (29) and (30). The weighted radiative and convective heat transfer coefficients of the interior surface nodes of the building elements h_{ci} and h_{ri} describe the conventional convective and radiative surface heat transfer coefficients for interiors and are taken to be constant. The interior surface convective heat transfer coefficient h_{ci} is constant and depends on the building type - 0.7 for the roof element, 2.5 for the external wall, glaze and internal mass elements and, 5.0 for the ground floor element. The interior surface radiative heat transfer coefficient is constant for all elements $h_{ri,el} = 5.13\,\mathrm{W\,m^{-2}\,K^{-1}}$.

3.4.2. Construction specifications

The ZEB-laboratory is built with a load bearing system of engineered wood. Column, beam and other structural parts are made of glue laminated timber. The stairwells and floors, elevator shafts and some interior walls are built with cross laminated timber. Exterior walls are made of a typical timber structure insulated with mineral wool. The construction specifications of the various elements of the building and their design U-values (thermal transmittance) are listed in Table 5.

3.4.3. Thermal properties

The normalized thermal resistance R of the building elements is obtained from Eq. (32), where $R_{gf,eog}$ represents the thermal resistance of ground floor including the effect of the ground and R_{gr} is the thermal resistance of a 0.5 m thick soil layer. $R_{gf,eog}$ and $h_{gr,vi}$ are calculated based on ISO 13370:2017 [40]. The normalized thermal properties of the elements, resistance and heat capacity κ_m, are distributed equally over the nodes of each element.

$$R_{el}(t) = \begin{cases} (r_{el} \cdot U_{el})^{-1} - (H_{ci,el} + H_{ri,el})^{-1} - (H_{se,el}(t))^{-1} & \text{if } el \neq gf \\ R_{gf,eog} + R_{gr} & \text{if } el = gf \end{cases} \tag{32}$$

3.4.4. Heat transfer

The heat delivered by the radiators ϕ_{rad} is computed using the non-linear equation in Eq. (33). A typical value of $n_{rad} = 1.3$ is taken for the radiator exponent. T_{lmtd} is the logarithmic mean temperature difference between the radiator panels and the internal air temperature T_{int}. The control signal for the radiator valves u_{rad} depends on the deviation of the internal air temperature at previous time step $T_{int}(t-1)$ to the desired indoor temperature $T_{int,set}$. It is modelled as a proportional controller with a proportional band $T_{rad,pb}$ of 1.5 °C.

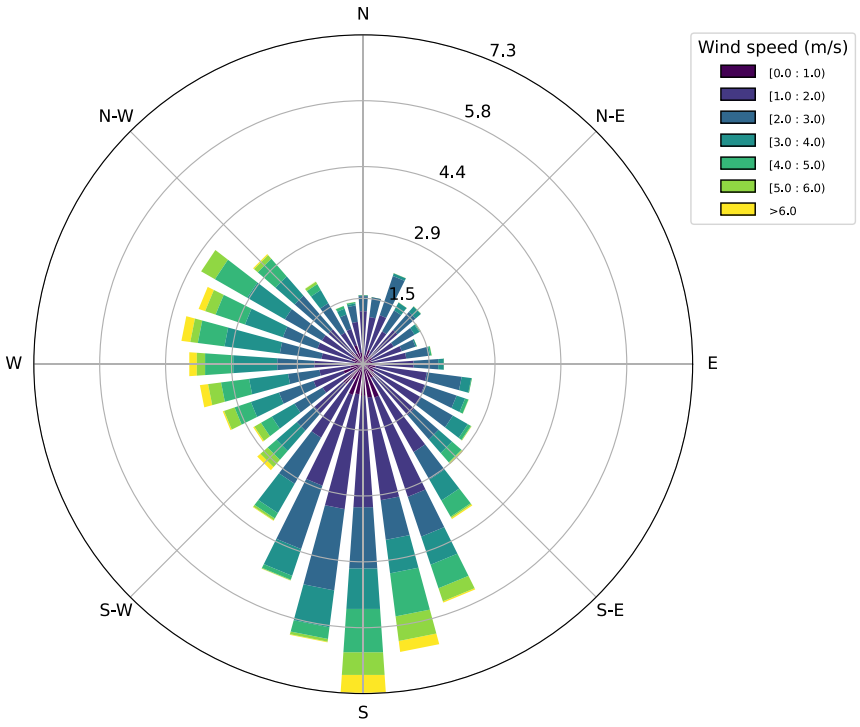

Fig. 10. Wind rose diagram of the local wind speed and direction at the ZEB-laboratory in 2022.

Table 5
Construction specifications of the elements of the ZEB-laboratory [41] along with their design thermal transmittance values.

Element	Material	Thickness (mm)	Thermal transmittance ($W\,m^{-2}\,K^{-1}$)
Ground floor	Concrete	100	0.10
	EPS insulation	250	
External wall	Timber cladding	22	0.15
	Ventilated gap	84	
	Timber frame wall and insulation	223	
	Insulation	73	
	Cladding/gypsum	13	
Internal mass	Chipboard	48	0.80
	Insulation	50	
	Wood	210	
Roof	PV system	104	0.09
	Ventilated gap	98	
	Plywood	21	
	I-beam with insulation	450	
	Gypsum	13	

$$\phi_{rad}(t) = u_{rad}(t) \cdot H_{rad} \cdot T_{lmtd}(t)^{n_{rad}} \tag{33}$$

$$T_{lmtd}(t) = \frac{T_{sup}(t) - T_{ret}(t)}{\ln\left(T_{sup}(t) - T_{int}(t-1)\right) - \ln\left(T_{ret}(t) - T_{int}(t-1)\right)} \tag{34}$$

$$u_{rad}(t) = 0.5 \cdot u_{rad}(t-1) + 0.5 \cdot \max\left[0, \min\left(\frac{1, T_{int,set} - T_{int}(t-1)}{T_{rad,pb}}\right)\right] \tag{35}$$

Normally, the supply temperature T_{sup} is determined based on a linear interpolation of a lookup table of $T_{sup,set}$ and T_e (external temperature) value pairs. However, for a predictive control scheme, the heat demand i.e. the heat delivered by the radiators for space-heating is required in-advance. This information is then used to optimize the schedule the operation of the thermal plant that delivers heat to the supply-line. Therefore, it is not possible to know T_{sup} and thus, the return temperature T_{ret}, in-advance. To overcome this challenge, the mean values of T_{sup} and T_{ret} measured during the operation of the thermal system are used.

The ventilation heat ϕ_{ve} delivered by the HRV unit is given by Eq. (36), where Q_{ve} is the specific air flow rate, η_{ve} is the heat recovery efficiency and $\kappa\rho_a = 1.21\,J\,m^{-3}\,K$ is the heat capacity of air per volume. The heat transfer due to infiltration ϕ_{inf} is affected by the external wind speed and temperature difference between internal and external air. It is estimated by using a modified form of the Alberta Air Infiltration Model (AIM-2) [42] to be suitable for large single zone models [43]. It is described in Eq. (37), where C_{inf} is the infiltration coefficient and the infiltration potential Q_{inf} accounts for both stack and wind effects.

$$\phi_{ve}(t) = \kappa\rho_a \cdot Q_{ve} \cdot (1 - \eta_{ve}) \cdot \left(T_{int}(t-1) - T_e(t)\right) \tag{36}$$

$$\phi_{inf}(t) = C_{inf} \cdot Q_{inf} \cdot \kappa\rho_a \cdot \left(T_{int}(t-1) - T_e(t)\right) \tag{37}$$

$$\phi_{sol}(t) = r_{gl} \cdot g_{gl} \cdot I_{tot,ver}(t) \tag{38}$$

Table 6
Parameters of the ZEB-laboratory RC network model.

Description	Parameter	Value
Building height	H	21.67 m
Building perimeter	P	86.3 m
Floor area	A_{fl}	440 m^2
Number of floors	N_{fl}	4
External wall azimuth angle	γ	[90, 180, 0, −90] °
External wall surface area fraction	F_{γ}	[0.18, 0.31, 0.31, 0.18]
Normalized heat capacity of roof	$\kappa_{m,rf}$	56 $Wh\,m^{-2}\,K^{-1}$
Normalized heat capacity of external walls	$\kappa_{m,ew}$	15 $Wh\,m^{-2}\,K^{-1}$
Normalized heat capacity of ground floor	$\kappa_{m,gf}$	56 $Wh\,m^{-2}\,K^{-1}$
Heat capacity of 0.5 m soil layer	κ_{gr}	280 $Wh\,m^{-2}\,K^{-1}$
Resistance of 0.5 m soil layer	R_{gr}	0.25 $K\,m^2\,W^{-1}$
Specific air flow rate	Q_{ve}	4.33 $m^3\,s^{-1}$
Heat recovery efficiency	η_{ve}	0.85
Infiltration coefficient	C_{inf}	0.081 $m^3\,s^{-1}\,Pa^{-1}$
Indoor temperature set-point	$T_{int,set}$	21 °C
Radiator constant	H_{rad}	0.66 $W\,m^{-2}\,K^{-1}$
Heat transfer due to thermal bridges	H_{tb}	0.04 $W\,m^{-2}\,K^{-1}$
Internal heat gains	ϕ_{int}	6.2 $W\,m^{-2}\,K^{-1}$

The ZEB-laboratory is equipped with triple glazed windows which are filled with argon. All the windows combined cover a total area of 488 m^2 which is about 27% of the total floor area. Solar heat gains due to absorbed solar radiation transmitted through the glazed windows is given in Eq. (38). The total solar irradiance on vertical surfaces $I_{tot,ver}$ is the weighted (by the surface area fraction F_{γ_k}) sum of the total irradiance on each vertical surface I_{tot,ver,γ_k} that is oriented at azimuth γ_k i.e. $I_{tot,ver} = \sum_k F_{\gamma_k} \cdot I_{tot,ver,\gamma_k}$. The python package *pvlib* [44] provides a useful method (pvlib.irradiance.get_total_irradiance) to calculate the total solar irradiance at an arbitrarily tilted and oriented surface based on solar irradiance components easily available from meteorological models. The U-value and solar transmittance of the window glaze elements are $U_{gl} = 0.8\,W\,m^{-2}\,K^{-1}$ and $g_{gl} = 0.45$ respectively.

Through Eq. (39), the radiant heat gains on exterior surfaces ϕ_{re} due to solar irradiation is obtained. Default values for the solar absorption coefficient $\alpha_{sol} = 0.5$ and the emissivity of surface $\epsilon = 0.9$ are used; σ is the Stefan–Boltzmann constant. The extra thermal radiation to the sky ϕ_{sky} in Eq. (40) depends on the temperature of the exterior surface node of the element and the surface thermal radiation downwards ϕ_{strd}.

$$\phi_{re,el}(t) = r_{el} \cdot \left(\alpha_{sol} \cdot I_{tot,hor}(t) - \phi_{sky,el}(t)\right) \tag{39}$$

$$\phi_{sky,el}(t) = F_{sky,el} \cdot \epsilon \cdot \left[\sigma \cdot T_{el}(t-1)^4 - \phi_{strd}(t)\right] \tag{40}$$

$$\phi_{ri,el}(t) = r_{el} \cdot \left[f_{r,sol} \cdot \phi_{sol,gl}(t) + f_{r,int} \cdot \phi_{int}(t) + f_{r,rad} \cdot \phi_{rad}(t)\right] \tag{41}$$

The radiant heat gains on interior surface of the element is expressed in Eq. (41), where f_r is the radiative fraction ($f_r = 1 - f_c$). The default convective fractions are [36]: $f_{c,sol} = 0.1$, $f_{c,int} = 0.4$ and $f_{c,rad} = 0.4$. Table 6 lists the various parameter of the thermal network model.

3.4.5. Weather data

The developed numerical model utilizes forecast weather data as boundary conditions to model the temperature dynamics as well as estimate the building energy needs. The required weather variables include wind speed, temperatures of the air and ground, and components of solar irradiation. They are retrieved from the following (open-)sources: Open-Meteo [45] and the ERA5-Land dataset of the Copernicus Climate Data Store (CDS) [46]. Table 7 displays the retrieved weather variables and their respective data sources.

3.4.6. Validation

The energy required to maintain the internal temperature of the building at the desired level comprises the space heating demand of the building ϕ_{sh}. In the developed model, it is equivalent to the energy delivered by the radiators and ventilators i.e. $\phi_{sh} = \phi_{rad} + \phi_{ve}$. In Fig. 11, the hourly heat demand estimates of the developed model are compared with measurement data over a week in November. It is observed that the developed numerical model is able to follow the heat demand profile of the building very closely. Further, an RMSE score of 3.4 kW for predictions over the week, shows that model is very reliable and accurate, considering that the maximum observed heat demand of the ZEB-laboratory is about 30 kW on the coldest days. It is also observed that, during the day-time peaks, the model is slightly over-predicting the energy demand of the building. Considering that the estimated heat demand profiles are input to the predictive control strategy to be developed for the PPTES unit, an over-prediction leads to an increased energy stored in the PPTES, while an under-prediction leads to, possibly, an insufficient amount of energy stored to satisfy the actual demand. Therefore, the developed numerical model is reliable and also highly computationally efficient, and is validated to be a useful tool for a predictive control strategy involving the PPTES.

Table 7
Weather forecast variables and their respective data sources.

Data source	Variable	Symbol
Open-Meteo [45]	Wind speed at 10 m	$U_{10\,m}$
	External temperature at 2 m	T_e
	Ground temperature at 1 m depth	T_{gr}
	Global horizontal irradiation	
	Diffuse solar irradiation	
	Direct normal irradiation	
ERA5-Land [46]	Surface thermal radiation downwards	ϕ_{strd}

4. Control strategy

In this section, the development of an optimal control strategy to optimize the charging schedule of the PPTES unit is discussed, and the numerical formulation is described. The performance of the optimal control is evaluated against an existing rule-based control strategy and the results are presented.

4.1. Reference control

A traditional rule-based feedback control based on temperature set-points and fixed charging schedules is currently the control strategy implemented in the ZEB-laboratory as a reference control to establish a performance benchmark.

The charge–discharge schedule for the PPTES is prescribed as follows: charge from heat pump during the night and discharge to building during early morning hours. During the rest of the day, the PPTES is on standby and the heat pump system delivers the required thermal energy directly to the building. In Fig. 12, the fixed schedule of the reference control is shown over a week.

4.2. Optimal control strategy

The developed optimal control strategy is a model-based predictive control strategy designed to optimally utilize the TES capability of the PPTES unit to shift the electrical load of the heat pump system and generate demand flexibility while satisfying the thermal needs of the ZEB-laboratory. The numerical formulation of the optimal control strategy as a discrete-time constrained-NLP (Non-Linear Programming) is given in Eq. (42a).

$$\underset{x_0,u_0,x_1\ldots u_{N-1},x_N}{\text{minimize}} \quad \sum_{k=0}^{N-1} L(x_k, u_k, w_k) \tag{42a}$$

$$\text{subject to} \quad x_{k+1} - f(x_k, u_k, w_k) = 0 \tag{42b}$$

$$h(x_k, u_k, w_k) \geq 0 \tag{42c}$$

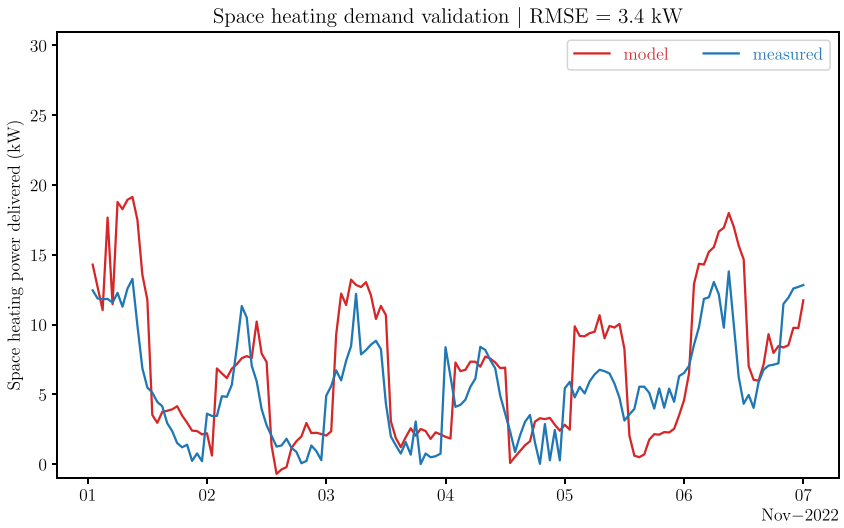

Fig. 11. Validation of the developed numerical model for space heating. The model estimates of the hourly space heating demand are plotted against the measured values over a week. The RMSE score of the model is 3.4 kW.

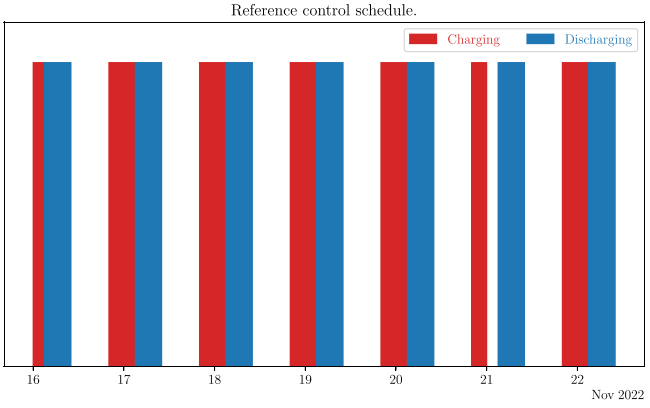

Fig. 12. Fixed schedule of the reference control strategy for the charging and discharging of the PPTES.

$$x_0 = x_{\text{ini}} \tag{42d}$$

$L(x_k, u_k)$ in Eq. (42a) is the cost function associated with step k of the prediction horizon, $f(x_k, u_k, w)$ is the system state function, $h(x_k, u_k, w)$ is the inequality constraint and w is the external input vector that acts as the decision variables for the solver. Table 8 lists the components of the external input vector. The temperature states of HTF, PCM, hot water tank T_{tank}, and the liquid fraction of the PCM together form the system state vector $x := [T_{\text{HTF}}\ T_{\text{PCM}}\ T_{\text{tank}}\ x_{\text{l, PCM}}]^{\text{T}}$. The control input vector, $u_k \in [0, 1]$, represents the flow rate of the pump that drives the PPTES. By controlling the pump flow rate, the charging schedule of the PPTES is optimized over the prediction horizon.

$$L(x_k, u_k) := P^k_{\text{HP}} \cdot \Delta t \cdot C^k_{\text{el}} \tag{43}$$

$$h(x_k, u_k, w) := E^k_{\text{PPTES}} - E^k_{\text{SH}} - E_{\text{buffer}} \tag{44}$$

The cost function in Eq. (43) is the energy cost of operating the heat pump system. P_{HP} is the power consumption, Δt is the control interval, and C_{el} is the day-ahead electrical market price obtained from Nordpool [47]. The inequality constraint in Eq. (44) ensures that there is always sufficient energy stored in the PPTES to satisfy the predicted space heating demand at all times. An energy buffer term ($E_{\text{buffer}} = 5$ kW h) is introduced to maintain an additional level of energy store to account for unforeseen surges in the heat demand.

In this formulation, the direct multiple shooting method is employed to decouple the integration of the system state dynamics and the optimization procedure [48]. The idea behind the multiple–shooting stems from the observation that accurately simulating (integrating) the system dynamics over long time periods is often difficult due to the propagation of non–linearity. Multiple–shooting seeks to tackle this issue by limiting the simulation to smaller time intervals *i.e.* the state function f is numerically integrated separately for each control interval $[t_k, t_{k+1}]$. Note that, in this approach, the optimization variables, control vector u and the state vector x, are discretized over the prediction horizon. The optimization problem (minimizing the objective function) and the state problem (integration of system states) are then solved simultaneously. Although, the inclusion of the state variables as optimization variables increases the dimension of the control problem, the complexity itself is significantly reduced due to the highly sparse nature of the Jacobian and Hessian matrices. The Jacobian matrix J and the Hessian matrix $\nabla_{x,u}\mathcal{L}^2$ of the Lagrangian $\mathcal{L}$ for the NLP in Eq. (42a) can be obtained from Eqs. (45)–(47). Fig. 13 illustrates the block-diagonal and sparse nature of the Jacobian matrix. This approach leads to the specially structured block-diagonal Jacobian and Hessian matrices which can be very efficiently solved by structure exploiting NLP solvers, such as IPOPT [49]. Further, it has been shown that this method is numerically stable and efficient, even for highly non-linear and chaotic systems [50].

$$J_p = \frac{\partial}{\partial p}\begin{bmatrix} [I]x_0 - x_{\text{ini}} \\ x_1 - f(x_0, u_0, w_0) \\ x_2 - f(x_1, u_1, w_1) \\ \vdots \\ x_{k+1} - f(x_k, u_k, w_k) \end{bmatrix} = \begin{cases} -\frac{\partial f(x_k, u_k, w_k)}{\partial p} & : \text{if } p = x_k \text{ or } p = u_k \\ 1 & : \text{if } p = x_{k+1} \\ 0 & : \text{otherwise} \end{cases} \tag{45}$$

$$\nabla_{x,u}\mathcal{L}^2 = \frac{\partial \mathcal{L}_k}{\partial x_i, u_j} = \begin{cases} \in \mathbb{R} & : \text{if } i = j = k \\ = 0 & : \text{if } i \neq j \neq k \end{cases} \tag{46}$$

$$\mathcal{L}_k = L_k(x_k, u_k, w_k) + \lambda_{k+1} \cdot \left(x_{k+1} - f(x_k, u_k, w_k)\right) \tag{47}$$

4.2.1. Flexibility indicators

Flexibility indicators are employed to quantify the amount of demand flexibility delivered by the delivered optimal control strategy. Energy flexibility is quantified by the available storage capacity C, defined in Eq. (48), which is a measure of amount of energy that is

Table 8
Components of the external input vector.

Variable	Description	Source	Unit
C_{el}	Day-ahead electricity price	Nordpool [47]	EUR/kW h
T_e	External temperature	Weather forecast	°C
E_{sh}	Predicted space heating demand	Heat demand model (Section 3.4)	kW h
x_{ini}	Initial system state	Measurement	°C
T_{amb}	Ambient room temperature	Measurement	°C

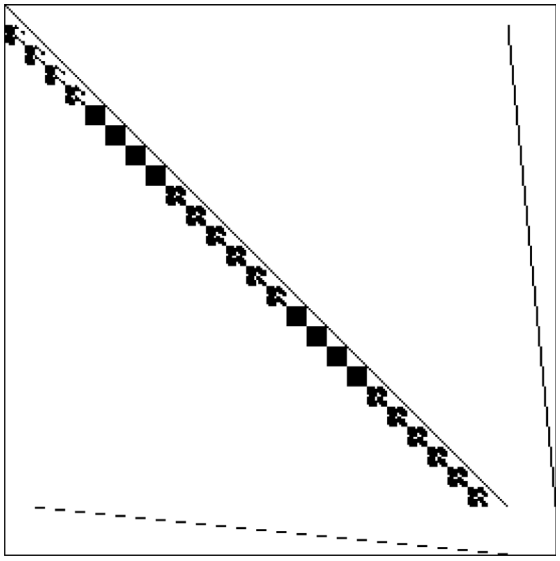

Fig. 13. Structure of the Jacobian matrix for a prediction horizon of 24 h.

shifted during optimal control. It is further split into upward C_{up} and downward C_{down} storage capacity. C_{up} (C_{down}) captures the demand increase (decrease) due to charging (discharging) events.

$$C = \sum_k (E^k_{OC} - E^k_{RC}) = C_{up} + C_{down} \tag{48}$$

$$C_{up} = \sum_k (E^k_{OC,\ up} - E^k_{RC,\ up}) \tag{49}$$

$$C_{down} = \sum_k (E^k_{OC,\ down} - E^k_{RC,\ down}) \tag{50}$$

Energy cost flexibility is quantified by the flexibility factor F, specified in Eq. (51), which accounts for low and high price periods. E is the total amount of energy consumption over the prediction horizon during high and low price periods. Periods are categorized as either high or low based on the price period exceeding by 1 standard deviation ($\mu \pm 1 \cdot \sigma$), assuming that the prices during the prediction window are normally distributed. The flexibility factor ranges from −1 (highly inflexible) to 1 (highly flexible system). $F = 1$ indicates that the system is operating at the highest possible flexibility. Energy cost savings and energy use reduction are calculated by Eqs. (52) and (53) respectively.

$$F = \frac{E_{\text{low price}} - E_{\text{high price}}}{E_{\text{low price}} + E_{\text{high price}}} \tag{51}$$

$$\text{Cost savings (\%)} = \frac{\sum_k (P^k_{HP,\ RC} - P^k_{HP,\ OC}) \cdot C^k_{el}}{\sum_k P^k_{HP,\ RC} \cdot C^k_{el}} \tag{52}$$

$$\text{Energy use reduction (\%)} = \frac{\sum_k (P^k_{HP,\ RC} - P^k_{HP,\ OC})}{\sum_k P^k_{HP,\ RC}} \tag{53}$$

4.2.2. Optimized charging schedule

In Figs. 14 and 15, the results of the optimal control strategy for prediction horizons of 48 and 24 hours are displayed. It can be observed that the charging schedule of the PPTES is optimized to reduce charging during high price periods and increase charging during low price periods. Further, the ability to shift demand is observed to be greater when the prediction horizon is 48 hours i.e. a longer prediction horizon provides a greater opportunity for the optimal controller to maximize the flexibility of the system by taking advantage of the information of externalities longer into the prediction horizon. Moreover, compared to the reference control, the energy consumption is significantly reduced while ensuring that there is always enough energy stored in the PPTES to satisfy the space heating demand. It is seen that the optimized charging profile maintains a balance between reducing energy consumption and satisfying energy demand while optimizing for maximal load shift capability.

The developed optimal control strategy is applied for an entire month in Winter 2022 and the results of the optimization are shown in Figs. 16 and 17 in terms of the above defined flexibility indicators. In comparison to the reference control, a sharp increase in the flexibility factor from near-zero and negative values to positive and almost unitary values is observed. It is a clear demonstration of the increase in system flexibility – from a not-so flexible to a highly flexible system – due to the optimal control strategy. The increase in flexibility factor is observed irrespective of the prediction horizon chosen, suggesting that the developed optimal controller is able to maximize the degree of flexibility available in the system regardless of the length of the prediction horizon.

Considering the storage capacity of the system, it is seen that the available average storage capacity per day is about 100 kW h–200 kW h and 50 kW h–150 kW h for prediction horizon of 48 and 24 hours respectively. However, most this storage capacity is available as downwards storage capacity due to the fact that reference control is over-consuming and over-charging during high price periods while the optimal control tries to reduce and distribute away this excess consumption.

The increase in flexibility of the system directly translates into significant reductions in both the energy usage and the energy cost of operation. Results show that the average reduction in energy use is about 45% while the average savings in energy cost is about 55%. The respective percentages are almost always greater than 20% on most days, showing the significant positive benefits of implementing the optimal control strategy. It is to be noted that on certain days, the energy reduction and cost savings are negative while the flexibility factor is positive. This can sometimes happen as increasing the flexibility of the system may not always go hand in hand with a decrease in energy consumption or reduction in energy cost.

Optimization results of the energy flexibility factor and the available storage capacity indicate that the developed optimal control strategy enables the ZEB-laboratory to transform itself into a flexible and dynamic building that can actively provide flexibility services to the grid on demand.

5. Conclusion

In this study, the design and development of an optimal control strategy for the operation of an innovative bio-wax based PPTES unit

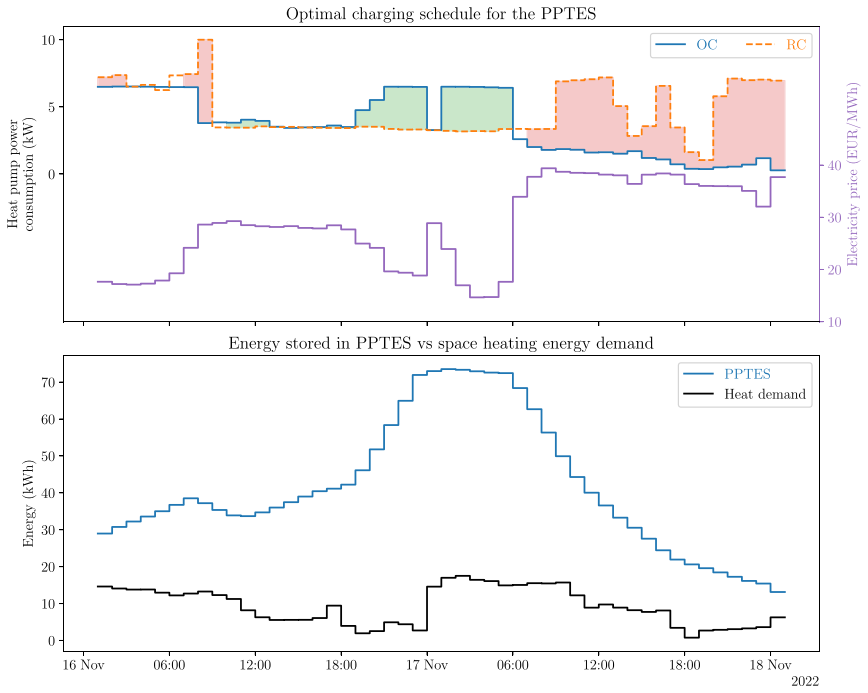

Fig. 14. Optimization results over a prediction horizon of 48 hours and control interval of 60 minutes. Top: Optimal charging schedule of the PPTES. Bottom: Energy stored and energy demand. Excess charging and reduced charging periods highlighted in green and red respectively.

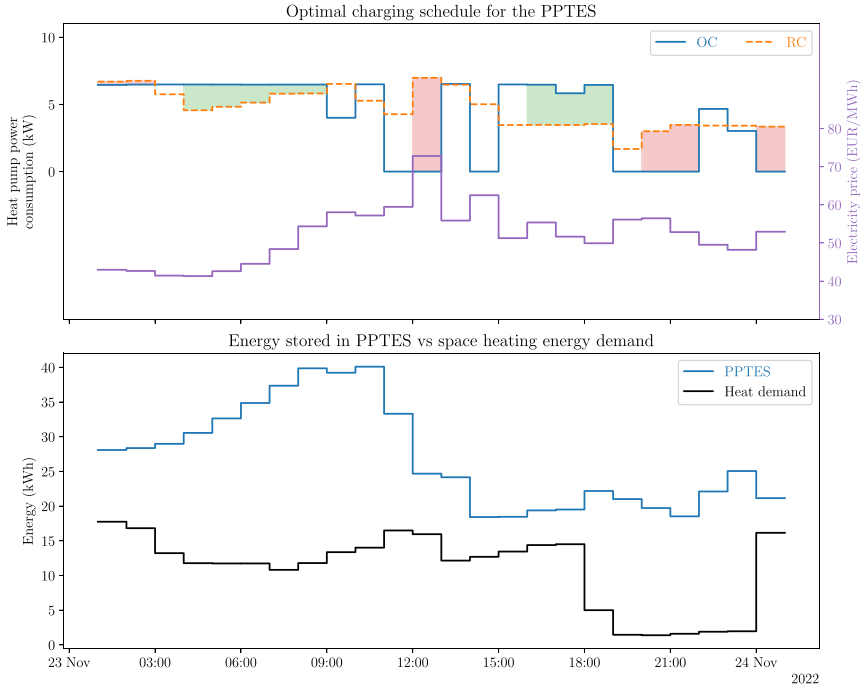

Fig. 15. Optimization results over a prediction horizon of 24 hours and control interval of 60 minutes. Top: Optimal charging schedule of the PPTES. Bottom: Energy stored and energy demand. Excess charging and reduced charging periods highlighted in green and red respectively.

delivering space heating to the four-storey-high research building, the ZEB-laboratory, is presented. The hydronic heating system in the ZEB-laboratory comprises an electric driven heat pump system and a PCM based PPTES unit on the primary side. The secondary side, comprises hydronic radiators and a ventilation unit that deliver space heating to the building. The primary side and secondary side are separated by a small hot water tank acting as a buffer between the supply and demand.

Numerical control-oriented dynamic model of the PPTES unit to simulate the phase-change dynamics of the PCM is developed and validated. Validation results show that the developed model achieves a high accuracy ($\pm 1\,^{\circ}C$) in simulating the temperature dynamics of the PCM and HTF during phase-change. Further, the thermal power delivered and the thermal energy stored are estimated by the model to a greater accuracy. In addition, a dynamic model for thermal stratification in the hot water tank and a data-driven regression model for the heat pump system are developed and validated against measurements. Thus, the developed models together are found to represent the thermal dynamics of the system to a sufficient degree of accuracy and are

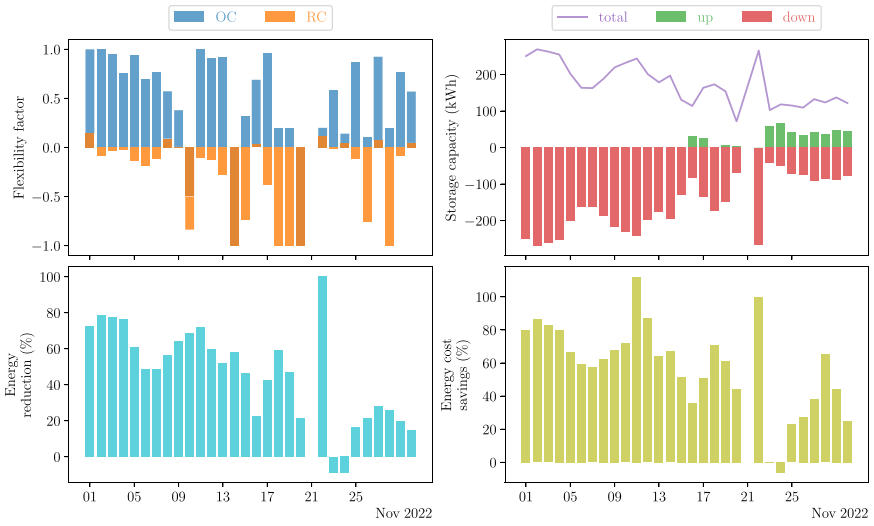

Fig. 16. Optimization results over a month in winter 2022. The prediction horizon is 48 hours and control interval is 60 minutes. Top left: Flexibility factor. Top right: Storage capacity, upward and downward storage capacity. Bottom left: Energy reduction. Bottom right: Energy cost savings.

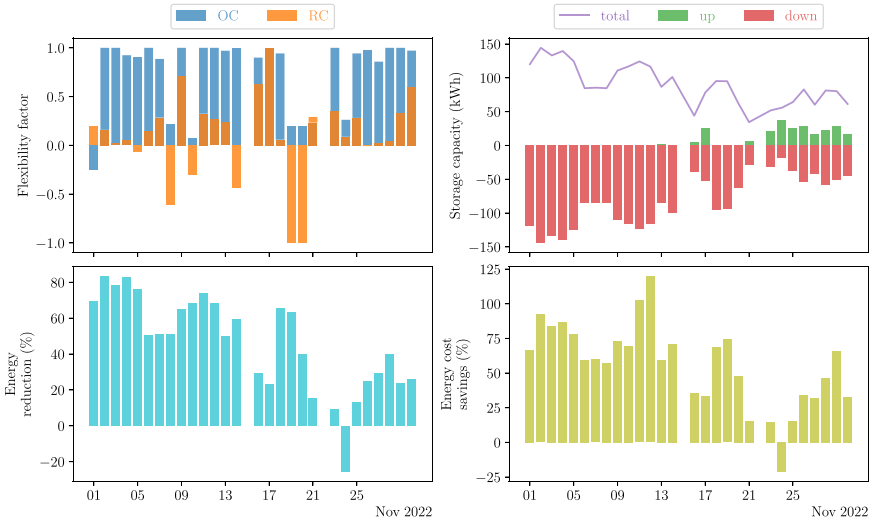

Fig. 17. Optimization results over a month in winter 2022. The prediction horizon is 24 hours and control interval is 60 minutes. Top left: Flexibility factor. Top right: Storage capacity, upward and downward storage capacity. Bottom left: Energy reduction. Bottom right: Energy cost savings.

suitable to be deployed in real-time predictive control applications.

A fast and reliable model to estimate the hourly space heating demand of the ZEB-laboratory is developed based on the 14-node RC thermal network model (ISO14N). The space heating model uses two inputs: building information data (physical properties, construction specifications) and weather forecast data. Validation results show that the developed model is able to estimate the observed space heating demand of the ZEB-laboratory with a good level of accuracy (RMSE score of 3.4 kW is achieved).

An optimal control strategy is designed for application in real-time operation of the PPTES unit. The validated component models are employed to predictively model the dynamics of the thermal system and the space heating model is utilized as a decision-support tool that provides information on the estimated space heating demand of the building in advance. The developed predictive control strategy is designed to optimally utilize the TES capability of the PPTES to generate demand flexibility by optimizing the charging scheduling of the PPTES through the heat pump system. The optimization responds to the time-varying electricity price vectors dynamically to shift demand away from high price periods while also ensuring that the space heating demand of the building is satisfied.

In comparison to the reference (a rule-based control), the developed optimal control strategy demonstrates a high degree of demand flexibility. Over a month of operation, the flexibility factor of the system is increased from negative values (inflexible system under the reference control) to values close to 1 (highly flexible system) consistently. Further, optimization results show the availability of storage capacity, mainly downshift regulation capacity in the range of 100 kW h–200 kW h, quantifying the capability of the optimized system to provide grid ancillary services and respond to up/down regulation requests on demand.

In addition to being demand flexible, the optimized charging schedules reduce the energy consumption and energy cost greatly. Results show consistent reduction in energy usage of about 20%–80% being obtained. Similarly, energy cost savings of 20%–110% are achieved. Therefore, the developed control strategy is highly efficient, both energy usage and cost wise, and demonstrates a significant capability to maximize the demand flexibility of thermal systems comprising power-to-heat unit such as a heat pump and a thermal energy store such as the PPTES unit.

CRediT authorship contribution statement

Aneesh Chandra Nunna: Writing – original draft, Visualization, Validation, Methodology, Data curation, Conceptualization. **Olav Galteland:** Writing – original draft, Visualization, Methodology, Conceptualization. **Laurent Georges:** Writing – review & editing, Supervision, Methodology, Conceptualization. **Yi Zong:** Writing – review & editing, Supervision, Methodology, Conceptualization.

Acknowledgements

The author, Aneesh Chandra Nunna, is supported by the Technical University of Denmark through the DTU Alliance PhD scholarship. Olav Galteland acknowledges the "Research Centre on Zero Emission Neighbourhoods in Smart Cities" granted by the Norwegian Research Council (No. 257660). Yi Zong gratefully acknowledges "Compact bio-based thermal energy storage for buildings" (ComBioTES) project granted by EU Horizon 2020 (No. 864496).

Declaration of competing interest

The authors declare that they have no known competing financial interests or personal relationships that could have appeared to influence the work reported in this paper.

Data availability

The authors do not have permission to share data.

References

[1] European Commission. The European green deal. 2020, Communication from the Commission to the European Parliament, the European Council, the Council, the European Economic and Social Committee and the Committee of the Regions.

[2] Hussain S, Lai C, Eicker U. Flexibility: Literature review on concepts, modeling, and provision method in smart grid. Sustain Energy Grids Netw 2023;35:101113. http://dx.doi.org/10.1016/j.segan.2023.101113, URL: https://www.sciencedirect.com/science/article/pii/S2352467723001212.

[3] Vandenbogaerde L, Verbeke S, Audenaert A. Optimizing building energy consumption in office buildings: A review of building automation and control systems and factors influencing energy savings. J Build Eng 2023;76:107233. http://dx.doi.org/10.1016/j.jobe.2023.107233, URL: https://www.sciencedirect.com/science/article/pii/S2352710223014134.

[4] Jensen SØ, Marszal-Pomianowska A, Lollini R, Pasut W, Knotzer A, Engelmann P, et al. IEA EBC annex 67 energy flexible buildings. Energy Build 2017;155:25–34. http://dx.doi.org/10.1016/j.enbuild.2017.08.044, URL: https://www.sciencedirect.com/science/article/pii/S0378778817317024.

[5] Pan Y, Zhu M, Lv Y, Yang Y, Liang Y, Yin R, et al. Building energy simulation and its application for building performance optimization: A review of methods, tools, and case studies. Adv Appl Energy 2023;10:100135. http://dx.doi.org/10.1016/j.adapen.2023.100135, URL: https://www.sciencedirect.com/science/article/pii/S2666792423000148.

[6] Kirkerud J, Nagel N, Bolkesjø T. The role of demand response in the future renewable northern European energy system. Energy 2021;235:121336. http://dx.doi.org/10.1016/j.energy.2021.121336, URL: https://www.sciencedirect.com/science/article/pii/S036054422101584X.

[7] Desguers T, Lyden A, Friedrich D. Integration of curtailed wind into flexible electrified heating networks with demand-side response and thermal storage: Practicalities and need for market mechanisms. Energy Convers Manage 2024;304:118203. http://dx.doi.org/10.1016/j.enconman.2024.118203, URL: https://www.sciencedirect.com/science/article/pii/S0196890424001444.

[8] Junker RG, Azar AG, Lopes RA, Lindberg KB, Reynders G, Relan R, et al. Characterizing the energy flexibility of buildings and districts. Appl Energy 2018;225:175–82. http://dx.doi.org/10.1016/j.apenergy.2018.05.037, URL: https://www.sciencedirect.com/science/article/pii/S030626191830730X.

[9] Aalto P, Haukkala T, Kilpeläinen S, Kojo M. Chapter 1 - Introduction: electrification and the energy transition. In: Aalto P, editor. Electrification. Academic Press; 2021, p. 3–24. http://dx.doi.org/10.1016/B978-0-12-822143-3.00006-8, URL: https://www.sciencedirect.com/science/article/pii/B9780128221433000068.

[10] Bloess A, Schill W-P, Zerrahn A. Power-to-heat for renewable energy integration: A review of technologies, modeling approaches, and flexibility potentials. Appl Energy 2018;212:1611–26. http://dx.doi.org/10.1016/j.apenergy.2017.12.073, URL: https://www.sciencedirect.com/science/article/pii/S0306261917317889.

[11] Østergaard DS, Smith KM, Tunzi M, Svendsen S. Low-temperature operation of heating systems to enable 4th generation district heating: A review. Energy 2022;248:123529. http://dx.doi.org/10.1016/j.energy.2022.123529, URL: https://www.sciencedirect.com/science/article/pii/S0360544222004327.

[12] Lund H, Werner S, Wiltshire R, Svendsen S, Thorsen JE, Hvelplund F, Mathiesen BV. 4Th generation district heating (4GDH): Integrating smart thermal grids into future sustainable energy systems. Energy 2014;68:1–11.

[13] Nunna AC, Zong Y, Thorsen JE. Demand side flexibility for a heat booster substation with ultra low temperature district heating. Sustain Energy Grids Netw 2023;36:101185. http://dx.doi.org/10.1016/j.segan.2023.101185, URL: https://www.sciencedirect.com/science/article/pii/S2352467723001935.

[14] Faraj K, Khaled M, Faraj J, Hachem F, Castelain C. Phase change material thermal energy storage systems for cooling applications in buildings: A review. Renew Sustain Energy Rev 2020;119:109579. http://dx.doi.org/10.1016/j.rser.2019.109579, URL: https://www.sciencedirect.com/science/article/pii/S1364032119307877.

[15] Nunna AC, Zong Y, Georges L, You S. Demand response with active phase change material based thermal energy storage in buildings. Energy Rep 2023;9:227–35. http://dx.doi.org/10.1016/j.egyr.2022.12.131, URL: https://www.sciencedirect.com/science/article/pii/S2352484722027330, 2022 The 3rd International Conference on Power, Energy and Electrical Engineering.

[16] Mehrizi AA, Karimi-Maleh H, Naddafi M, Karimi F. Application of bio-based phase change materials for effective heat management. J Energy Storage 2023;61:106859. http://dx.doi.org/10.1016/j.est.2023.106859, URL: https://www.sciencedirect.com/science/article/pii/S2352152X23002566.

[17] Aftab W, Usman A, Shi J, Yuan K, Qin M, Zou R. Phase change material-integrated latent heat storage systems for sustainable energy solutions. Energy Environ Sci 2021;14:4268–91. http://dx.doi.org/10.1039/D1EE00527H.

[18] Nazir H, Batool M, Bolivar Osorio FJ, Isaza-Ruiz M, Xu X, Vignarooban K, et al. Recent developments in phase change materials for energy storage applications: A review. Int J Heat Mass Transfer 2019;129:491–523. http://dx.doi.org/10.1016/j.ijheatmasstransfer.2018.09.126, URL: https://www.sciencedirect.com/science/article/pii/S0017931018324578.

[19] Okogeri O, Stathopoulos VN. What about greener phase change materials? A review on biobased phase change materials for thermal energy storage applications. Int J Thermofluids 2021;10:100081. http://dx.doi.org/10.1016/j.ijft.2021.100081, URL: https://www.sciencedirect.com/science/article/pii/S2666202721000197.

[20] Mastani Joybari M, Selvnes H, Vingelsgård E, Sevault A, Hafner A. Parametric study of low-temperature thermal energy storage using carbon dioxide as the phase change material in pillow plate heat exchangers. Appl Therm Eng 2023;221:119796. http://dx.doi.org/10.1016/j.applthermaleng.2022.119796, URL: https://www.sciencedirect.com/science/article/pii/S1359431122017264.

[21] Kathirgamanathan A, De Rosa M, Mangina E, Finn DP. Data-driven predictive control for unlocking building energy flexibility: A review. Renew Sustain Energy Rev 2021;135:110120. http://dx.doi.org/10.1016/j.rser.2020.110120, URL: https://www.sciencedirect.com/science/article/pii/S1364032120304111.

[22] Lopes RA, Chambel A, Neves J, Aelenei D, Martins J. A literature review of methodologies used to assess the energy flexibility of buildings. Energy Procedia 2016;91:1053–8. http://dx.doi.org/10.1016/j.egypro.2016.06.274, URL: https://www.sciencedirect.com/science/article/pii/S1876610216303745, Proceedings of the 4th International Conference on Solar Heating and Cooling for Buildings and Industry (SHC 2015).

[23] Finck C, Li R, Kramer R, Zeiler W. Quantifying demand flexibility of power-to-heat and thermal energy storage in the control of building heating systems. Appl Energy 2018;209:409–25. http://dx.doi.org/10.1016/j.apenergy.2017.11.036, URL: https://www.sciencedirect.com/science/article/pii/S0306261917316112.

[24] Tarragona J, Pisello AL, Fernández C, de Gracia A, Cabeza LF. Systematic review on model predictive control strategies applied to active thermal energy storage systems. Renew Sustain Energy Rev 2021;149:111385. http://dx.doi.org/10.1016/j.rser.2021.111385, URL: https://www.sciencedirect.com/science/article/pii/S1364032121006705.

[25] Wei Z, Calautit J. Evaluation of model predictive control (MPC) of solar thermal heating system with thermal energy storage for buildings with highly variable occupancy levels. In: Building simulation, vol. 16, (10):Springer; 2023, p. 1915–31.

[26] Cao Y, Du J, Soleymanzadeh E. Model predictive control of commercial buildings in demand response programs in the presence of thermal storage. J Clean Prod 2019;218:315–27. http://dx.doi.org/10.1016/j.jclepro.2019.01.266, URL: https://www.sciencedirect.com/science/article/pii/S0959652619302914.

[27] Nocente A, Time B, Mathisen H, Kvande T, Gustavsen A. The ZEB laboratory: the development of a research tool for future climate adapted zero emission buildings. J Phys Conf Ser 2021;2069(1):012109. http://dx.doi.org/10.1088/1742-6596/2069/1/012109.

[28] Sevault A, Næss E. Active latent heat storage using biowax in a central heating system of a ZEB living lab. In: Proceedings of the 14th IIR-gustav Lorentzen conference on natural refrigerants. IIR; 2020.

[29] Galteland O, Gouis M, Salgado Beceiro J, Sevault A. Fourteen months operation of a 200 kwh latent heat storage pilot. 2023, p. 1–5. http://dx.doi.org/10.23919/SpliTech58164.2023.10193589.
[30] Croda Industrial Specialties. Crodatherm 37 data sheet. 2024.
[31] Sevault A, Salgado Beceiro J, Bjørgen KO. 200-kWh latent heat storage unit using a pillow-plate heat exchanger: demonstration in an office building. In: 15th IIR-gustav Lorentzen conference on natural refrigerants, trondheim, Norway, June 13-15th 2022. IIR; 2022, p. 190–232. http://dx.doi.org/10.18462/iir.gl2022.0063.
[32] Architizer. ZEB laboratory. 2020, URL: https://architizer.com/projects/zeb-laboratory-1/.
[33] Zhan R, Zhang B, Liu L, Huan C, Zhao D, Xi H. An improved equivalent heat capacity method to simulate and optimize latent thermal energy storage units. Int J Heat Mass Transfer 2024;235:126135. http://dx.doi.org/10.1016/j.ijheatmasstransfer.2024.126135, URL: https://www.sciencedirect.com/science/article/pii/S0017931024009657.
[34] Försterling S, Selvnes H, Sevault A. Validation of a modelica numerical model for pillow plate heat exchangers using phase change material. In: 15th IIR-gustav Lorentzen conference on natural refrigerants, trondheim, Norway, June 13-15th 2022. IIR; 2022.
[35] Lundström L, Akander J, Zambrano J. Development of a space heating model suitable for the automated model generation of existing multifamily buildings—A case study in nordic climate. Energies 2019;12(3). http://dx.doi.org/10.3390/en12030485, URL: https://www.mdpi.com/1996-1073/12/3/485.
[36] Danish Standards Association. Energy performance of buildings - energy needs for heating and cooling, internal temperatures and sensible and latent heat loads - Part 1: Calculation procedures. 2017.
[37] Liu J, Heidarinejad M, Gracik S, Srebric J. The impact of exterior surface convective heat transfer coefficients on the building energy consumption in urban neighbourhoods with different plan area densities. Energy Build 2015;86:449–63. http://dx.doi.org/10.1016/j.enbuild.2014.10.062, URL: https://www.sciencedirect.com/science/article/pii/S0378778814009086.
[38] Kennedy HE. ASHRAE handbook - Fundamentals. 2021.
[39] Danish Standards Association. Energy performance of buildings - calculation of energy use for space heating and cooling. 2008.
[40] Danish Standards Association. Thermal performance of buildings - heat transfer via the ground - calculation methods. 2017.
[41] Søraas AEH. Building performance simulation of the new ZEB Laboratoriet. Norwegian University of Science and Technology; 2020.
[42] Walker IS, Wilson DJ. Field validation of algebraic equations for stack and wind driven air infiltration calculations. HVAC R Res 1998;4(2):119–39. http://dx.doi.org/10.1080/10789669.1998.10391395.
[43] Hayati A, Mattsson M, Sandberg M. Evaluation of the LBL and AIM-2 air infiltration models on large single zones: 3 historical churches. Build Environ 2014;81:365–79. http://dx.doi.org/10.1016/j.buildenv.2014.07.013.
[44] Anderson KS, Hansen CW, Holmgren WF, Jensen AR, Mikofski MA, Driesse A. pvlib python: 2023 project update. J Open Source Softw 2023;8(92):5994. http://dx.doi.org/10.21105/joss.05994.
[45] Open-Meteo. Open-meteo: An open-source weather API. 2024, URL: https://open-meteo.com/.
[46] Copernicus Climate Data Store. ERA5-land hourly data.. 2024, URL: https://cds.climate.copernicus.eu.
[47] Nordpool. Nordpool hourly day-ahead electricity spot price market. 2022, URL: https://www.nordpoolgroup.com/.
[48] Kouzoupis D, Pendharkar I, Frey J, Diehl M, Corman F. Direct multiple shooting for computationally efficient train trajectory optimization. Transp Res C 2023;152:104170. http://dx.doi.org/10.1016/j.trc.2023.104170, URL: https://www.sciencedirect.com/science/article/pii/S0968090X23001596.
[49] Biegler L, Zavala V. Large-scale nonlinear programming using IPOPT: An integrating framework for enterprise-wide dynamic optimization. Comput Chem Eng 2009;33(3):575–82. http://dx.doi.org/10.1016/j.compchemeng.2008.08.006, URL: https://www.sciencedirect.com/science/article/pii/S0098135408001646.
[50] Bock HG, Diehl MM, Leineweber DB, Schlöder JP. A direct multiple shooting method for real-time optimization of nonlinear DAE processes. In: Allgöwer F, Zheng A, editors. Nonlinear model predictive control. Basel: Birkhäuser; 2000, p. 245–67.